Chinese Physics Letters **42**, 080712 (2025) **Express Letter**

Strain-Induced One-Dimensional Magnetic Stripe in Metallic Monolayer H-$NbSe_2$

Liangguang Jia(贾亮广)[1†], Can Zhang(张璨)[1†], Fei Gao(高飞)[2†], Yaoyao Chen(陈瑶瑶)[1], Lili Zhou(周丽丽)[1], Fudi Zhou(周福迪)[1], Xu Han(韩旭)[1], Teng Zhang(张腾)[1], Daniel Sánchez-Portal[3], Shiwu Gao(高世武)[4], Yu Zhang(张钰)[1,5*], and Yeliang Wang(王业亮)[1*]

[1]*School of Integrated Circuits and Electronics, MIIT Key Laboratory for Low-Dimensional Quantum Structure and Devices, Beijing Institute of Technology, Beijing 100081, China*
[2]*Donostia International Physics Center (DIPC), 20018 Donostia-San Sebastián, Spain*
[3]*Centro de Física de Materiales (CFM) CSIC-UPV/EHU, E-20018 Donostia-San Sebastián, Spain*
[4]*Beijing Computational Science Research Center, Beijing 100193, China*
[5]*Advanced Research Institute of Multidisciplinary Sciences, Beijing Institute of Technology, Beijing 100081, China*

(Received 18 May 2025; accepted manuscript online 4 July 2025)

Lattice distortion of materials has a profound impact on their electronic and magnetic properties, which can generate local magnetic states in intrinsically non-magnetic systems. Here we report on the realization of a one-dimensional (1D) magnetic stripe in monolayer H-$NbSe_2$ sustained by strain along the terraces of the graphene/SiC substrates. The strength of this tensile strain is widely tunable by the height-to-width ratio of the terraces. Increasing the tensile strength leads to the shifts and splitting of the Nb 4d bands crossing the Fermi energy, generating spin polarization in a 1D magnetic stripe along the terrace. Simultaneously, the charge-density-wave signature of strained H-$NbSe_2$ is significantly suppressed. Such a magnetic stripe can be locally quenched by an individual Se-atom defect via the defect-induced Jahn–Teller distortion and charge density redistribution. These findings provide a different route to achieving and manipulating 1D magnetism in otherwise non-magnetic systems, offering a new way for spintronic devices.

DOI: 10.1088/0256-307X/42/8/080712 CSTR: 32039.14.0256-307X.42.8.080712

Realization of magnetism in atomically thin materials, accompanied by their unique electronic and optical properties, is expected to open up new opportunities for spintronic devices.[1–4] Pristine two-dimensional materials are usually non-magnetic; lattice distortions and atomic defects are known to generate magnetic responses due to local atomic rearrangements or change of external environments, which lead to localized magnetic states and novel magnetism governed by new physical principles.[5,6] To reach this goal, one promising strategy is to fabricate van der Waals heterostructures combining the magnetic and non-magnetic building blocks, where the magnetism can be introduced in the non-magnetic component owing to the proximity effect.[7,8] However, such a magnetism is always extrinsic and usually absent in the individual components of the systems.

Intrinsic magnetism in graphene with specially engineered configurations has triggered an avalanche of research over the last decade. Pristine graphene has linear energy-momentum dispersion relations crossing at the Dirac point. The current paradigms of graphene magnetism rely on a core concept of introducing electronic states close to the Fermi level E_F. For example, adsorption of individual H chemisorption and creating carbon vacancies in graphene have been demonstrated to generate spin-polarised quasilocalized states at the E_F, creating a local magnetic moment in graphene. This local magnetism can be attributed to the Coulomb repulsion of π electrons[9,10] and the in-plane π–σ exchange interaction.[11–13] Another example is nanographenes or graphene nanoribbons with zigzag edge topologies, where the spin polarization of low-energy edge states is expected to be triggered through the Coulomb repulsion.[14,15]

For non-magnetic transition metal dichalcogenides (TMDs), density functional theory (DFT) calculations have predicted that a local magnetic moment can be introduced by creating metal vacancies (Pt vacancies in $PtSe_2$[16,17] and Re vacancies in ReS_2[18]) or chalcogen-metal antisites (substitutional Mo atoms at Te sites in $MoTe_2$[19] and substitutional W atoms at S sites in WS_2[20]) at the nanoscale. Alternatively, strain engineering has also been theoretically investigated as a promising route to realize magnetism, especially in TMD metals including $NbSe_2$, NbS_2, and $TaSe_2$.[21–23] However, owing to the complex interaction between atomic morphology and the emerged spin polarization, the realization of a tunable magnetic system in low dimensions and the understanding of the derived magnetism in non-magnetic TMDs remain a formidable challenge in ongoing research.

In this work, we report the evidence of strain-induced

†These authors contributed equally to this work.
*Corresponding authors. Email: yzhang@bit.edu.cn; yeliang.wang@bit.edu.cn
© 2025 Chinese Physical Society and IOP Publishing Ltd. All rights, including for text and data mining, AI training, and similar technologies, are reserved.

one-dimensional (1D) magnetic stripes in monolayer H-$NbSe_2$ supported on architected terraces by means of scanning tunneling microscopy (STM) measurements combined with DFT calculations. A tensile strain can be controllably introduced in the monolayer H-$NbSe_2$ by placing it on top of graphene/SiC substrates with variable and well-characterized terraces. As the tensile strain is increased, the Nb 4d bands crossing the E_F initially shift to a higher energy and then split into two spin-polarized states, yielding a 1D magnetic stripe along the terrace. Moreover, an individual Se-atom defect can locally quench such a magnetism because of the Jahn–Teller distortion and charge density redistribution. Considering the unique control of 1D magnetic stripe via terrace strain and defect, our findings are promising for establishing strained monolayer H-$NbSe_2$ as a new platform for spin transport devices.

In our experiments, large-scale monolayer H-$NbSe_2$ was synthesized onto epitaxial bilayer-graphene-terminated 4H-SiC(0001) substrates via a molecular beam epitaxy (MBE) method,[24,25] as depicted in Fig. 1(a). There are plenty of terraces in SiC with heights ranging from 0.25 to 1.20 nm [Fig. S1 in the Supplementary Materials (SM)], owing to the miscut of wafers from the (0001) direction.[26,27] The atomic arrangement of $NbSe_2$ is intact and continuous, roughly following the morphology of substrates across the terraces, which can be directly visualized via large-scale and atomic-resolution STM images shown in Fig. 1(b) and Fig. S2 of the SM. In this scenario, $NbSe_2$ on top of a SiC step edge is expected to undergo uniaxial tensile strain along the direction perpendicular to the edge,[28,29] with the strain strength strongly dependent on the gradient of the height profile

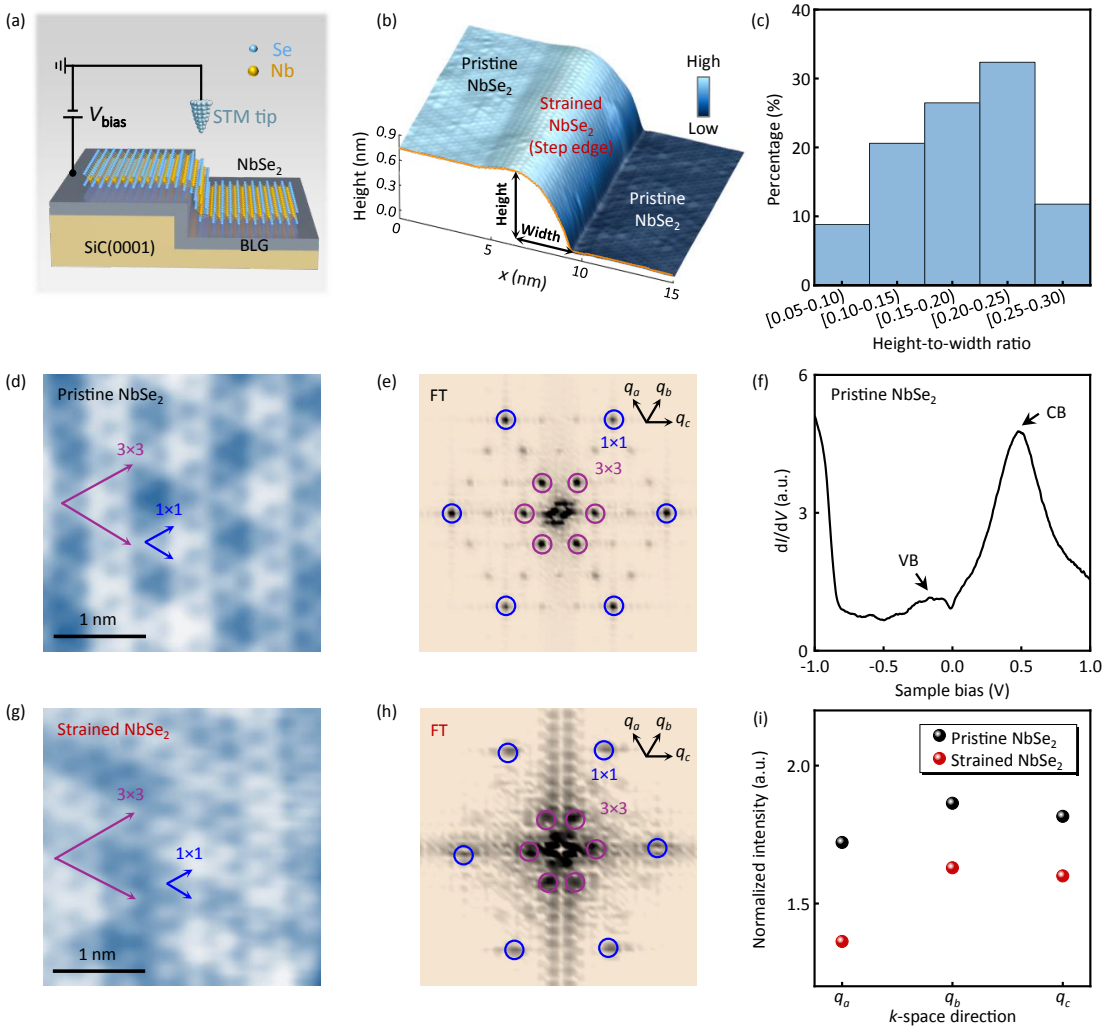

Fig. 1. Construction of strained monolayer $NbSe_2$. (a) Schematic representation of constructing monolayer $NbSe_2$ under a tensile strain by means of bilayer-graphene-terminated 4H-SiC(0001) with step edges. (b) STM image of $NbSe_2$ on top of a step edge ($V_s = -0.6$ V, $I_t = 0.1$ nA). The orange line shows the height profile exhibited in STM image, with the height and width of the strained region labeled in the panel. (c) The distribution of height-to-width ratios collected from several tens of cases. (d) Atomic-resolution STM image of pristine $NbSe_2$ away from step edges ($V_s = -0.5$ V, $I_t = 0.2$ nA). (e) FT image of pristine $NbSe_2$ in panel (d). The outer and inner bright spots, marked by the blue and red circles, represent the Bragg lattice and 3×3 CDW superlattice, respectively. (f) STS spectrum recorded on pristine $NbSe_2$ away from step edges. (g) Atomic-resolution STM image of strained $NbSe_2$ on top of a step edge ($V_s = -0.5$ V, $I_t = 0.2$ nA). (h) FT image of strained $NbSe_2$ in panel (g). (i) Normalized CDW peak intensities along the three lattice directions acquired from FT images.

exhibited in STM image[30,31] [Fig. 1(b) and Fig. S3 of the SM]. In our cases, the strained monolayer $NbSe_2$ are typically 2.7 to 6.9 nm width by examining tens of individual regions, yielding height-to-width ratios within 0.05 to 0.30, as summarized in Fig. 1(c).

Figures 1(d) and 1(g) show atomically resolved STM images of monolayer $NbSe_2$ on graphene-covered SiC substrates, complementary with the corresponding Fourier transform (FT) images given in Figs. 1(e) and 1(h), respectively. For pristine $NbSe_2$ away from the step edges, the top Se atoms dominate the images, producing a well-defined 3×3 charge-density-wave (CDW) configuration[25,32] [Figs. 1(d) and 1(e)]. When $NbSe_2$ is subjected to a tensile strain by placing it on top of step edges [Figs. 1(g) and 1(h)], the intrinsic CDW order is efficiently suppressed, which can be straightforwardly captured from the summarization of normalized CDW peak intensities presented in FT images [Fig. 1(i)]. The normalization was performed by dividing the intensity of the CDW peaks by those of the corresponding atomic Bragg peaks in the same direction. Similar phenomena have been observed in many cases, which help us rule out any possible artifacts. Considering that the CDW configuration of monolayer $NbSe_2$ is mainly caused by the Nb in-plane displacements,[33,34] the extended Nb-Nb interatomic distances under tensile strain are responsible for the weakened CDW signature.

We now focus on the electronic properties of monolayer $NbSe_2$ under tensile strain. For comparison, we firstly carry out dI/dV (STS) measurements of pristine $NbSe_2$, as typically shown in Fig. 1(f). There are two pronounced density of states (DOS) peaks appearing at the sample biases of about 0.5 V and −0.2 V, corresponding to the conduction band (CB) and valence band (VB) of pristine $NbSe_2$ respectively, which are in agreement with previous studies.[25,35] Strikingly, the dI/dV spectra of $NbSe_2$ on graphene-covered SiC step edges exhibit significantly distinct characteristics and are extremely sensitive to the strain strength. By measuring dozens of individual cases, we find that the evolution of strain-driven electronic properties in $NbSe_2$ can be classified into two categories, namely case 1 (small strain) and case 2 (large strain), which can be roughly distinguished by the height-to-width ratios that are smaller and larger than 0.24, respectively.

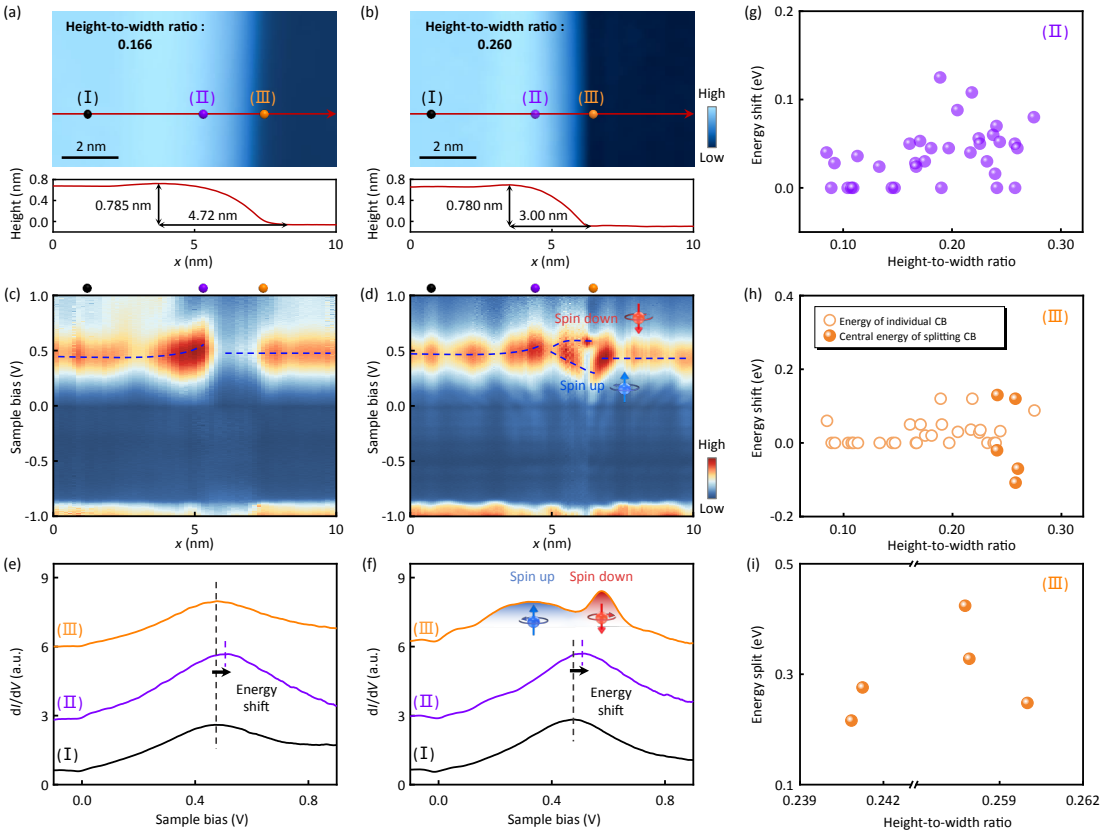

Fig. 2. Electronic properties of monolayer $NbSe_2$ under a tensile strain. (a, b) STM images of monolayer $NbSe_2$ under two representative strained regions with the height-to-width ratios of 0.166 (case 1) and 0.260 (case 2), respectively ($V_s = -0.6$ V, $I_t = 0.1$ nA). (c, d) Spatially resolved dI/dV spectra recorded across the step edges along the red arrows in panels (a) and (b). (e, f) Typical dI/dV spectra recorded at the positions I (pristine region, marked by the black sphere), Ⅱ (on the step towards the edge, marked by the purple sphere), and Ⅲ (at the step slope, marked by the orange sphere). Under a small height-to-width ratio (case 1), the C_1 peak shifts towards a higher energy as approaching the step edge. While under a large height-to-width ratio (case 2), the C_1 peak first shifts towards a higher energy and then splits into two DOS peaks. (g) Energy shift of the C_1 peak acquired at position Ⅱ relative to position I as a function of height-to-width ratio. (h) Energy shift of the C_1 peak acquired at position Ⅲ relative to position I as a function of height-to-width ratio. For case 2, the C_1 peak energy is regarded as the average energy of the two peaks. The hollow and solid circles represent the energy shifts of cases 1 and 2, respectively. (i) Energy separations of the two spin-polarized peaks in case 2 as a function of height-to-width ratio.

Figures 2(c) and 2(d) display the spatially resolved dI/dV spectra of $NbSe_2$ recorded across the step edges for these two cases typically shown in Figs. 2(a) and 2(b), with the height-to-width ratios of approximately 0.166 and 0.260, respectively. For the former of applying a small tensile strain on $NbSe_2$, the CB peak gradually shifts to higher energy as measured on the step towards the edge (position Ⅱ, marked by the purple sphere), accompanied by an increased electron density. At the step slope (position Ⅲ, marked by the orange sphere), however, the CB peak is markedly weakened, with its energy nearly equivalent to that of pristine $NbSe_2$ (position I, marked by the black sphere), which can also be deduced from the extracted STS spectra given in Fig. 2(e). In contrast, for the latter case of applying a large tensile strain, in addition to the CB peak shifting upwards as approaching the step edge, the CB peak prefers to split into two DOS peaks at the step slope [Figs. 2(d) and 2(f)], which, to the best of our knowledge, has not been reported before. However, the split features cannot be observed below the E_F (Fig. S4 of the SM). This is because the STS signals below the E_F in $NbSe_2$ are extremely low since they mainly originate from the in-plane Nb d orbitals, thus preventing the detection. The CB peak splitting is the main experimental finding of this paper and can be further confirmed as the strain-induced spin polarization in $NbSe_2$.

To systemically investigate the strained-induced evolution of the electronic states in $NbSe_2$, we summarize the CB evolution as a function of the height-to-width ratio ranging from 0.05 to 0.30, as summarized in Figs. 2(g)–2(i). At the step edge (position Ⅱ) shown in Fig. 2(g), the CB peak shifts to a higher energy of about (0.05 ± 0.03) eV for 62% cases, independent of the height-to-width ratio. However, at the step slopes (position Ⅲ) shown in Fig. 2(h), the CB peak remains almost unchanged when the height-to-width ratio is smaller than 0.15, and then shifts upwards as the ratio increases. When the ratio exceeds 0.24, the CB peak splits into two DOS peaks with an energy separation of about 0.30 eV, as presented in Fig. 2(i).

In order to uncover the underlying physics, we carry out the rigorous DFT calculations. Here the CDW configuration of monolayer $NbSe_2$ is not considered for simplicity, since it has negligible influence on the main results. For pristine monolayer $NbSe_2$ in the absence of tensile strain, the hybridization between Nb 4d and Se 4p orbitals contributes to the strong covalent bonds, with each Se atom gaining 0.7 electron. Consequently, the magnetism of Nb atoms is quenched,[24] yielding highly delocalized Nb 4d bands crossing the E_F. As exhibited in Fig. S5 of the SM, the Nb d_{z^2} orbital prevails near Γ above the E_F and is primarily responsible for the observed CB peak in our STS measurements, while the Nb $d_{x^2-y^2}$ and d_{xy} orbitals mainly concentrate around K.

For strained $NbSe_2$, we establish a rectangular supercell consisting of two Nb atoms and four Se atoms. A tensile strain is applied along the x direction, which corresponds to the $NbSe_2$ armchair edges marked in the inset of Fig. 3(a), closely aligned with experiments in Fig. S2 of the SM. Figure 3(a) illustrates the evolution of non-spin-constrained bands along Γ–X under different tensile

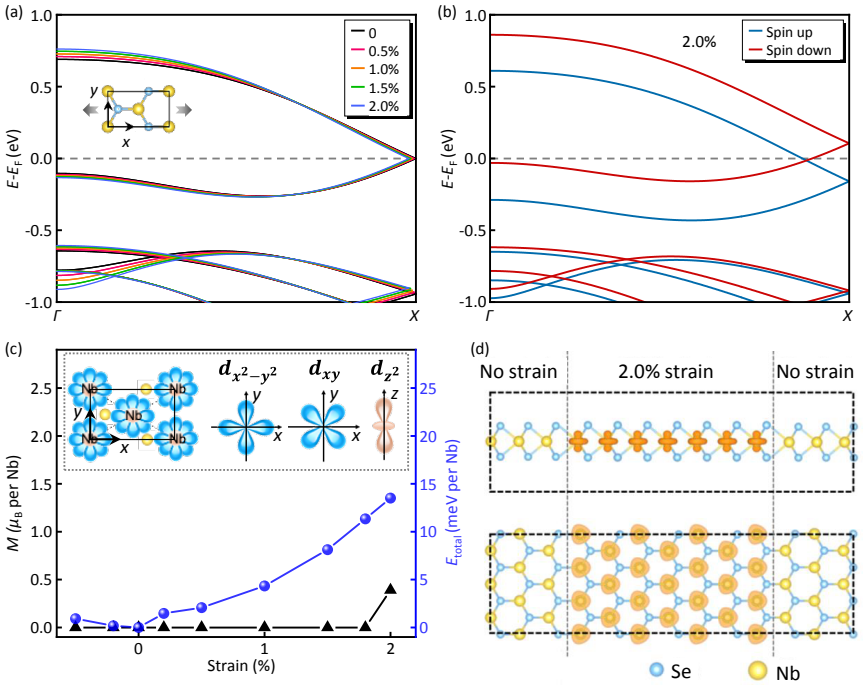

Fig. 3. DFT calculations of the electronic band structures in monolayer $NbSe_2$ under x-direction strain. (a) Evolution of non-spin-constrained bands in monolayer $NbSe_2$ along Γ–X under different tensile strains. Inset: a rectangular supercell consisting of two Nb atoms and four Se atoms. A tensile strain is applied along x direction that corresponds to the $NbSe_2$ armchair edges. (b) Spin-polarized band structure of $NbSe_2$ under a 2.0% tensile strain. The blue and red lines indicate the spin-up and spin-down components, respectively. (c) Calculated magnetism moment and energy cost of $NbSe_2$ as a function of strain. (d) Spin density of $NbSe_2$ under a 2.0% tensile strain in 1D. The orange cloud represents spin-up electrons with the isosurface of $\pm 0.005\, e\text{A}^{-3}$.

strains. It is evident that the band near Γ, locating around 0.7 eV, prefers to shift upwards by several tens of meV as the strain increases, in accordance with our experiments of case 1 (small height-to-width ratio) shown in Fig. 2(c).

The spin-polarized simulations exhibited in Fig. 3(b) further indicate that, as the tensile strain exceeds 2.0%, monolayer $NbSe_2$ becomes magnetic, where the partially filled Nb 4d bands split into two spin-polarized states with the energy separation of about 0.26 eV, much larger than those away from the E_F. Simultaneously, the occupied Se p_{xy} band shifts downwards to stabilize such magnetic states. Similar phenomena are also observed by applying a 2.0% tensile strain along the zigzag direction (Figs. S6 and S7 of the SM), implying that the strain-induced spin polarization in $NbSe_2$ is robust. Therefore, we can apparently attribute the experimentally observed CB peak splitting [case 2, large height-to-width ratio, see Fig. 2(d)] to the two spin-polarized states, highlighting the realization of a magnetism in monolayer $NbSe_2$ via strain engineering. Additionally, the widths and intensities of the two split peaks are spatially dependent.

Figure 3(c) summarizes the calculated magnetism moment and energy cost of $NbSe_2$ as a function of strain. As tensile strain is applied, the covalent bond length becomes longer, thus weakening the orbital coupling between Nb and Se atoms, which is expected to result in a magnetic ground state. On the contrary, $NbSe_2$ remains nonmagnetic under a compressive strain. At the critical point of phase transition, the distance between the two neighboring Nb atoms in a supercell increases by 0.053 Å. Meanwhile, the Nb-Se bond length along the x direction increases slightly by 0.017 Å, while the other inequivalent Nb-Se bond remains almost unchanged. Such a configuration incurs an energy cost of 13.9 meV per Nb atom, suggesting both electronic and magnetic characteristics of $NbSe_2$ are highly sensitive to the atomic geometry. The calculated spin density of $NbSe_2$ under a 2.0% tensile strain, shown in Fig. 3(d), reveals that the Nb d_{z^2} orbital mainly contributes to the net spin, with a spin moment of 0.35 μ_B per Nb atom.

Previous experiments have widely demonstrated that atomic defects host the ability to modify the magnetic

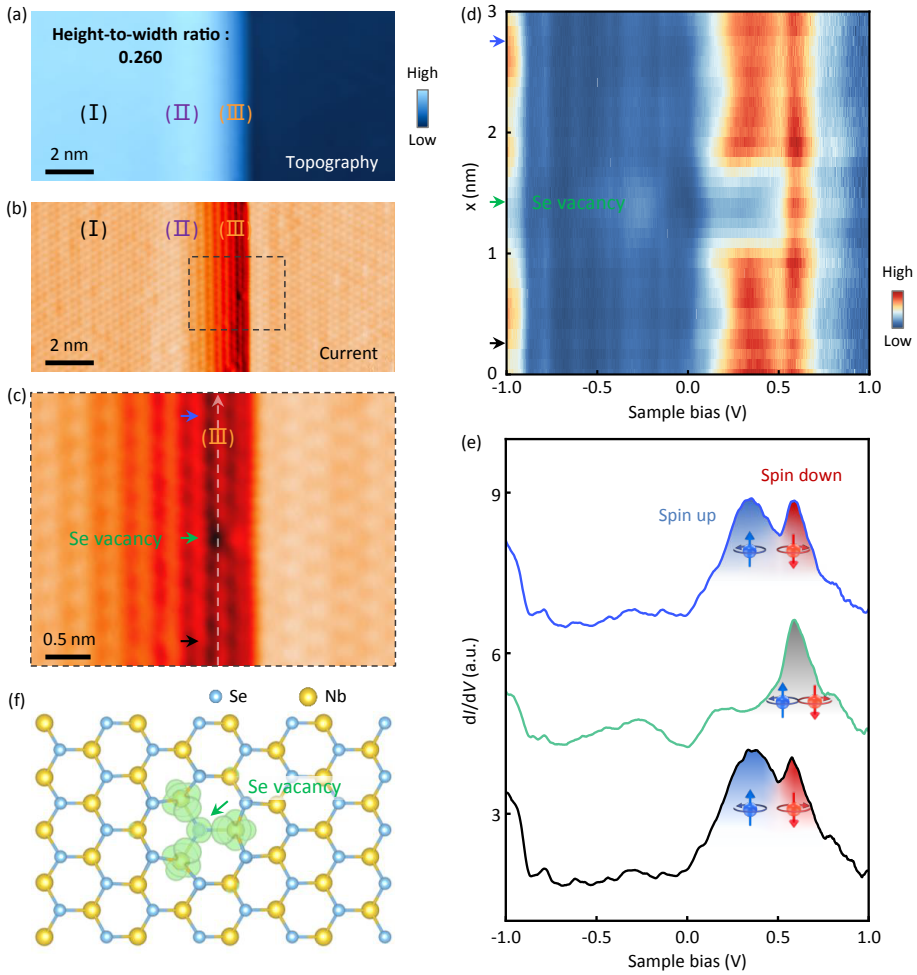

Fig. 4. Manipulation of magnetic state in strained monolayer $NbSe_2$ via an individual Se vacancy. (a) STM topography images of monolayer $NbSe_2$ on a bilayer-graphene-covered SiC(0001) step edge with the height-to-width ratio of 0.260 ($V_s = -0.6$ V, $I_t = 0.1$ nA). (b) Corresponding current image recorded at the same region as panel (a). (c) Zoomed-in current image of the dashed gray rectangle in panel (b). A Se vacancy can be clearly identified, as marked by the green arrow. (d) Spatially resolved dI/dV spectra recorded across the Se vacancy along the dashed arrow marked in panel (c). (e) Representative dI/dV spectra recorded at the marked locations in panels (c) and (d). (f) Charge density distribution of an individual Se vacancy in strained $NbSe_2$.

ground state of materials.[36–38] However, the underlying physical mechanism remains controversial due to the lack of atomically resolved examination. In the following, we provide the evidence that the strain-induced magnetic moment in monolayer $NbSe_2$ can be precisely manipulated via an individual Se vacancy. Figures 4(a) and 4(b) show representative STM topography and current images of strained $NbSe_2$ on a graphene-covered SiC step edge with a height-to-width ratio of 0.26 (case 2). An individual Se vacancy is located at the step slope[39] (position Ⅲ), which can be identified as a dark point in the magnified current image of Fig. 4(c). From the spatially resolved $\mathrm{d}I/\mathrm{d}V$ spectra exhibited in Figs. 4(d) and 4(e), we can observe that the biases of strain-induced two spin-polarized peaks in $NbSe_2$ are robust along the step slope, while the intensity of the low-energy peak is significantly suppressed around the Se vacancy, yielding only one resonance peak near the E_F (STS maps are given in Fig. S8 of the SM). Such a phenomenon directly indicates that the strain-induced magnetism in $NbSe_2$ can be locally quenched via an individual Se vacancy.

To gain deeper insights into the origin of such magnetic manipulation, we perform the DFT calculation modeled by a 3×6 supercell of monolayer $NbSe_2$ with a central Se vacancy under a 2.0% tensile strain along the armchair direction (see Methods). As shown in Fig. 4(f), there are obvious Jahn–Teller distortion (the distance between the nearest Nb atoms increases to about 4.1 Å) and electron accumulation at the vacancy site, which is mainly derived from the Nb 4d orbitals.[39,40] In contrast to the unstrained system, a Se atom vacancy in strained $NbSe_2$ can relax the local geometry, thus efficiently reducing the local strain. Therefore, the unpaired electrons of the nearby Nb atoms in strained $NbSe_2$ can be partially neutralized, yielding a quenched magnetic moment localized around the vacancy.[41,42] Our calculated spin-resolved DOS given in Fig. S9 of the SM further confirms that the two spin-polarized DOS peaks of strained $NbSe_2$ tend to be degenerate around the Se vacancy, which is responsible for the reduced total magnetic moment. These results well reproduce the main features of the measured STS spectra presented in Figs. 4(d) and 4(e), highlighting the experimental realization and manipulation of 1D magnetic stripe in monolayer $NbSe_2$ via the terrace strain and defects.

In summary, we successfully generated a 1D magnetic stripe in intrinsically non-magnetic monolayer $NbSe_2$ by applying a terrace tensile strain and realized the manipulation of this magnetic state at the nanoscale via Se-atom defects. Combining STM experiments and DFT calculations, we propose that the unusual Nb 4d bands crossing the E_F dominate such a magnetic phase transition. The magnetism in strained $NbSe_2$ stems from the weakened covalent interactions between the Nb 4d orbitals and Se 4p orbitals. An individual Se vacancy can generate Jahn–Teller distortion and charge density redistribution, which partially neutralizes the unpaired electrons and thus quenches the magnetic moment of Nb 4d orbitals. Our findings provide new insights into generating and manipulating magnetism in non-magnetic systems, paving the way for spintronic devices.

Methods.

Sample Preparation. Monolayer $NbSe_2$ preparation and STM/STS measurements were carried out in a STM system (USM-1300, Unisoku). Bilayer graphene was epitaxially grown by the thermal decomposition of 4H-SiC (0001) at 1200 ℃ for 45 min. Then, high-quality monolayer $NbSe_2$ was synthesised onto BLG/SiC(0001) via an MBE method. Selenium atoms (Sigma, 99.999%) were evaporated from a Knudsen cell, and Niobium atoms (ESPI Metals, 99.999%) were evaporated from an electron-beam evaporator; they were deposited onto the graphene-covered SiC(0001) substrate maintained at 500 ℃. The deposition ratio of Se to Nb was approximately 10:1 to ensure a rich Se environment. The growth rate of $NbSe_2$ is 0.002 ML/min. After the growth, a post-annealing process was performed at 300 ℃ to desorb the excess Se.

STM/STS Measurements. The STM/STS measurements were carried out under a base pressure of 1×10^{-10} mbar at 4.2 K. An electrochemically etched tungsten tip was used as the STM probe, which was calibrated by using a standard graphene lattice and a Si(111) (7×7) lattice. All the STM images were measured inconstant current mode. The STS measurements were taken using a standard lock-in technique with the bias modulation of 5 mV at 973 Hz.

DFT Calculations. DFT calculations were performed via Vienna *ab initio* simulation package (VASP)[43] with projector augmented wave method (PAW).[44,45] We adopted the GGA-PBE4[46,47] for exchange-correlation and used a plane-wave cutoff of 600 eV to expand the wave functions. $NbSe_2$ was modeled by both a 1×1 rectangular supercell with a K-point mesh of $18 \times 36 \times 1$ and a 3×6 supercell with a K-point mesh of $6 \times 6 \times 1$. $NbSe_2$ with a Se vacancy was modeled by a 3×6 supercell under a 2.0% strain along the armchair direction. All atoms were allowed to relax until the force on each atom less than 0.001 eV/Å for the 1×1 supercell and 0.05 eV/Å for the 3×6 supercell. In addition, a 20 Å thick vacuum layer was introduced for all the models.

Acknowledgements. This work was supported by the National Key R&D Program of China (Grant Nos. 2022YFA1402602, 2022YFA1402502, 2021YFA1400103, 2020YFA0308802, and 2024YFA1611300), the National Natural Science Foundation of China (Grant Nos. 92163206, 12274026, 12321004, 12304205, 11934003, 12393831, and U2230402), Beijing Association for Science and Technology Youth Talent Lift Program, MCIN/AEI/10.13039/501100011033 (Grant No. PID2022-140845OB-C66), and FEDER Una manera de hacer Europa.

References

[1] Gong C, Li L, Li Z L, Ji H W, Stern A, Xia Y, Cao T, Bao W, Wang C Z, Wang Y, Qiu Z Q, Cava R J, Louie S G, Xia J, and Zhang X 2017 *Nature* **546** 265

[2] Huang B, Clark G, Navarro-Moratalla E, Klein D R, Cheng R, Seyler K L, Zhong D, Schmidgall E, McGuire M A, Cobden D H, Yao W, Xiao D, Jarillo-Herrero P, and Xu X D 2017 *Nature* **546** 270

[3] Burch K S, Mandrus D, and Park J G 2018 *Nature* **563** 47
[4] Mak K F, Shan J, and Ralph D C 2019 *Nat. Rev. Phys.* **1** 646
[5] Zhou H X, Holleis L, Saito Y, Cohen L, Huynh W, Patterson C L, Yang F Y, Taniguchi T, Watanabe K, and Young A F 2022 *Science* **375** 774
[6] Grover S, Bocarsly M, Uri A, Stepanov P, Battista G D, Roy I, Xiao J W, Meltzer A Y, Myasoedov Y, Pareek K, Watanabe K, Taniguchi T, Yan B H, Stern A, Berg E, Efetov D K, and Zeldov E 2022 *Nat. Phys.* **18** 885
[7] Zhong D, Seyler K L, Linpeng X Y, Wilson N P, Taniguchi T, Watanabe K, McGuire M A, Fu K M C, Xiao D, Yao W, and Xu X D 2020 *Nat. Nanotechnol.* **15** 187
[8] Matsuoka H, Habe T, Iwasa Y, Koshino M, and Nakano M 2022 *Nat. Commun.* **13** 5129
[9] González-Herrero H, Gómez-Rodríguez J M, Mallet P, Moaied M, Palacios J J, Salgado C, Ugeda M M, Veuillen J Y, Yndurain F, and Brihuega I 2016 *Science* **352** 437
[10] Yazyev O V and Helm L 2007 *Phys. Rev. B* **75** 125408
[11] Zhang Y, Li S Y, Huang H Q, Li W T, Qiao J B, Wang W X, Yin L J, Bai K K, Duan W H, and He L 2016 *Phys. Rev. Lett.* **117** 166801
[12] Zhang Y, Gao F, Gao S W, and He L 2020 *Sci. Bull.* **65** 194
[13] Gao F, Zhang Y, He L, Gao S W, and Brandbyge M 2021 *Phys. Rev. B* **103** L241402
[14] Mishra S, Beyer D, Eimre K, Kezilebieke S, Berger R, Gröning O, Pignedoli C A, Müllen K, Liljeroth P, Ruffieux P, Feng X L, and Fasel R 2020 *Nat. Nanotechnol.* **15** 22
[15] Li J C, Sanz S, Corso M, Choi D J, Peña D, Frederiksen T, and Pascual J I 2019 *Nat. Commun.* **10** 200
[16] Avsar A, Ciarrocchi A, Pizzochero M, Unuchek D, Yazyev O V, and Kis A 2019 *Nat. Nanotechnol.* **14** 674
[17] Avsar A, Cheon C Y, Pizzochero M, Tripathi M, Ciarrocchi A, Yazyev O V, and Kis A 2020 *Nat. Commun.* **11** 4806
[18] Horzum S, Çakır D, Suh J, Tongay S, Huang Y S, Ho C H, Wu J, Sahin H, and Peeters F M 2014 *Phys. Rev. B* **89** 155433
[19] Guguchia Z, Kerelsky A, Edelberg D, Banerjee S, von Rohr F, Scullion D, Augustin M, Scully M, Rhodes D A, Shermadini Z, Luetkens H, Shengelaya A, Baines C, Morenzoni E, Amato A, Hone J C, Khasanov R, Billinge S J L, Santos E, Pasupathy A N, and Uemura Y J 2018 *Sci. Adv.* **4** eaat3672
[20] Li W F, Fang C M, and van Huis M A 2016 *Phys. Rev. B* **94** 195425
[21] Zhou Y G, Wang Z G, Yang P, Zu X T, Yang L, Sun X, and Gao F 2012 *ACS Nano* **6** 9727
[22] Manchanda P, Sharma V, Yu H B, Sellmyer D J, and Skomski R 2015 *Appl. Phys. Lett.* **107** 032402
[23] Chowdhury S, Simpson J R, Einstein T L, and Hight Walker A R 2019 *Phys. Rev. Mater.* **3** 084004
[24] Xi X X, Wang Z F, Zhao W W, Park J H, Law K T, Berger H, Forró L, Shan J, and Mak K F 2016 *Nat. Phys.* **12** 139
[25] Ugeda M M, Bradley A J, Zhang Y, Onishi S, Chen Y, Ruan W, Ojeda-Aristizabal C, Ryu H, Edmonds M T, Tsai H Z, Riss A, Mo S K, Lee D, Zettl A, Hussain Z, Shen Z X, and Crommie M F 2015 *Nat. Phys.* **12** 92
[26] Yazdi G R, Vasiliauskas R, Iakimov T, Zakharov A, Syväjärvi M, and Yakimova R 2013 *Carbon* **57** 477
[27] Ming F and Zangwill A 2011 *Phys. Rev. B* **84** 115459
[28] Nigge P, Qu A C, Lantagne-Hurtubise É, Mårsell E, Link S, Tom G, Zonno M, Michiardi M, Schneider M, Zhdanovich S, Levy G, Starke U, Gutiérrez C, Bonn D, Burke S A, Franz M, and Damascelli A 2019 *Sci. Adv.* **5** eaaw5593
[29] Aljarb A, Fu J H, Hsu C C, Chuu C P, Wan Y, Hakami M, Naphade D R, Yengel E, Lee C J, Brems S, Chen T A, Li M Y, Bae S H, Hsu W T, Cao Z, Albaridy R, Lopatin S, Chang W H, Anthopoulos T D, Kim J, Li L J, and Tung V 2020 *Nat. Mater.* **19** 1300
[30] Georgi A, Nemes-Incze P, Carrillo-Bastos R, Faria D, Kusminskiy S V, Zhai D W, Schneider M, Subramaniam D, Mashoff T, Freitag N M, Liebmann M, Pratzer M, Wirtz L, Woods C R, Gorbachev R V, Cao Y, Novoselov K S, Sandler N, and Morgenstern M 2017 *Nano Lett.* **17** 2240
[31] Wang G R, Dai Z H, Xiao J K, Feng S Z, Weng C X, Liu L Q, Xu Z P, Huang R, and Zhang Z 2019 *Phys. Rev. Lett.* **123** 116101
[32] Gye G, Oh E, and Yeom H W 2019 *Phys. Rev. Lett.* **122** 016403
[33] Lian C S, Si C, and Duan W H 2018 *Nano Lett.* **18** 2924
[34] Oh E, Gye G, and Yeom H W 2020 *Phys. Rev. Lett.* **125** 036804
[35] Zhang Q Z, Fan J H, Zhang T, Wang J Z, Hao X Y, Xie Y M, Huang Z P, Chen Y Y, Liu M, Jia L G, Yang H X, Liu L W, Huang H Q, Zhang Y, Duan W H, and Wang Y L 2022 *Commun. Phys.* **5** 117
[36] Yun S J, Cho B W, Dinesh T, Yang D H, Kim Y I, Jin J W, Yang S H, Nguyen T D, Kim Y M, Kim K K, Duong D L, Kim S G, and Lee Y H 2022 *Adv. Mater.* **34** 2106551
[37] Liang Q J, Zhang Q, Zhao X X, Liu M Z, and Wee A T S 2021 *ACS Nano* **15** 2165
[38] Cai L, He J F, Liu Q H, Yao T, Chen L, Yan W S, Hu F C, Jiang Y, Zhao Y D, Hu T D, Sun Z H, and Wei S Q 2015 *J. Am. Chem. Soc.* **137** 2622
[39] Jia L G, Gao F, Zhang Y, Chen Y Y, Hou B F, Huang Z P, Zhang Q Z, Wu X, Liu L W, Gao S W, Brandbyge M, Gao H J, and Wang Y L 2023 *Nano Res.* **16** 5715
[40] Nguyen L, Komsa H P, Khestanova E, Kashtiban R J, Peters J J P, Lawlor S, Sanchez A M, Sloan J, Gorbachev R V, Grigorieva I V, Krasheninnikov A V, and Haigh S J 2017 *ACS Nano* **11** 2894
[41] Wickramaratne D, Haim M, Khodas M, and Mazin I I 2021 *Phys. Rev. B* **104** L060501
[42] Wickramaratne D and Mazin I I 2022 *Nat. Commun.* **13** 2376
[43] Kresse G and Hafner J 1993 *Phys. Rev. B* **47** 558
[44] Vanderbilt D 1990 *Phys. Rev. B* **41** 7892
[45] Blöchl P E 1994 *Phys. Rev. B* **50** 17953
[46] Wang Y and Perdew J P 1991 *Phys. Rev. B* **44** 13298
[47] Perdew J P, Burke K, and Ernzerhof M 1996 *Phys. Rev. Lett.* **77** 3865